Article

Biospectroscopy of nanodiamond-induced alterations in conformation of intra- and extracellular proteins – a nanoscale IR study

Dipesh Khanal, Alexey Kondyurin, Herman Hau, Jonathan C. Knowles, Olga Levinson, Iqbal Ramzan, Dong Fu, Curtis Marcott, and Wojciech Chrzanowski

Just Accepted

Biospectroscopy of nanodiamond-induced alterations in conformation of intra- and extracellular proteins – a nanoscale IR study

Dipesh Khanal,[†] Alexey Kondyurin,[‡] Herman Hau,[†] Jonathan C. Knowles,[⁞] Olga Levinson,[ʊ] Iqbal Ramzan,[†] Dong Fu,[†] Curtis Marcott,[§] Wojciech Chrzanowski[*,†, ¡]

†Faculty of Pharmacy, The University of Sydney, NSW 2006, Australia

‡School of Physics, The University of Sydney, NSW 2006, Australia

§Light Light Solutions, P. O. Box 81486, Athens, GA 30608-1484, USA

⁞Division of Biomaterials and Tissue Engineering, UCL Eastman Dental Institute, University College London, 256 Gray's Inn Road, London WC1X 8LD, UK

ʊRay Techniques Ltd., Jerusalem, 9139101, Israel

¡Australian Institute of Nanoscale Science and Technology, The University of Sydney, NSW 2006, Australia

ABSTRACT: The toxicity of nanomaterials raises major concerns because of the impact that nanomaterials may have on health, which remains poorly understood. We need to explore the fate of individual nanoparticles in cells at nano and molecular levels to establish their safety. Conformational changes in secondary protein structures are one of the main indicators of impaired biological function and hence, the ability to identify these changes at a nanoscale level offers unique insights into the nanotoxicity of materials. Here, we used nanoscale infrared spectroscopy and demonstrated for the first time that nanodiamonds induced alterations in both extra- and intracellular secondary protein structures, leading to the formation of antiparallel β-sheet, β-turns, intermolecular β-sheet and aggregation of proteins. These conformational changes of the protein structure may result in the loss of functionality of proteins and in turn lead to adverse effects.

INTRODUCTION

Nanomaterials, which are present virtually everywhere in cosmetics, toiletries, food products, medical imaging systems and therapeutic agents[1-5], raises increasing safety concerns. As highlighted by a number of studies, nanoparticles are readily taken up by cells *via* different active or passive pathways, primarily through phagocytosis, pinocytosis and endocytosis[6-9]. However, the mechanisms and pathways involved in the uptake of different types of nanoparticles are complex and may be dependent on a number of factors such as their size[10,11], surface chemistry, charge, geometry or shape[11-13], and also vary from cell to cell[14-16]. The disparity in properties and uptake mechanisms affects the localization of these nanoparticles and interactions with cells and tissues. Therefore, there is a pressing need to explore the fate of individual nanoparticles at both the cellular and molecular level.

Interactions between nanoparticles and cells are highly dependent on nanoparticle–protein and nanoparticle–macromolecule interactions. Proteins may be in the form of structural proteins (e.g. tubulin, actin), cell signaling molecules (e.g. hormones) or even enzymes. Slight changes in the conformation of these proteins may lead to alteration or even complete loss of their functionality. It is well documented that nanoparticles have high affinity for proteins, which depends on their physicochemical properties including size, charge and shape[17]. Nanoparticle–protein interactions may result in changes in the conformation of proteins[18,19]. For instance,

Figure 1. Schematic representation of AFM-IR spectroscopy: conformational changes in the protein structure occurred after exposure to nanodiamond particles. Formation of antiparallel β-sheet was detected around the region of nanoparticle localization whereas non treated cells had high α-helical content.

Quantum dots have been reported to induce significant decrease in α-helical content of human adult hemoglobin [20]. Similarly, gold and polystyrene particles lead to decreased α-helix and increased β-turn structures in bovine serum albumin[18,21]. It is thus critical to gain a precise knowledge on how do nanoparticles interact with both intra- and extracellular proteins and whether these interactions disrupt protein conformations. Nanoparticles have comparable sizes to proteins, and thus may interfere with the cell signaling processes or impair protein function. In addition, nanoparticles may inadvertently be in-

volved in chaperone-like activity, which is vital for controlling protein folding during their assembly. This means that the interference of protein folding by nanoparticles may lead to the formation of peptide aggregates or peptide fibrils that have amyloid-like structures[19,22], which are known to be linked to neurodegenerative diseases such as Alzheimer's disease[19,22].

Commonly, to investigate *in vitro* nanotoxicity conventional spectrofluorometric and spectrophotometric assays, which employ fluorescent dyes or proteins, are used. Because of specific physicochemical properties and high reactivity of nanoparticles, they can bind and interact with the dye and the assay proteins[23]. These interactions were reported to adversely affect the fluorescence and/or the absorbance characteristics of indicator molecules[23]. Altered fluorescence/absorbance introduces a bias to the results and makes these assays ineffective for the toxicity assessment. To overcome the limitations of conventional assays, biospectroscopy has emerged as a promising tool to investigate nanotoxicity and to assess the interactions of biomolecules, such as proteins, with materials and nanomaterials[24-26]. Typically, biospectroscopy involves the use of non-invasive techniques including Raman spectroscopy[25,26], Fourier transform infrared spectroscopy (FTIR), circular dichroism spectroscopy, surface plasmon resonance and X-ray crystallography[18,27-29]. These methods allow us to detect the effect of nanoparticles on proteins at macro and micron levels[24]. However, all these techniques have limited sensitivity and spatial resolution. The micron-level resolution may not provide sufficiently detailed information on the effect of individual nanoparticle on cellular proteins. For example, the lateral resolution of the FTIR technique ranges up to 24 μm[30] in the mid-IR range, which is much too large to identify the subtle differences or structural changes resulting from interactions between individual nanoparticles and proteins at a nanoscale[31,32]. In addition, FTIR spectra collected from the bulk material may not actually represent the chemical fingerprint of the sample at the nano level.

Recently, Dazzi[33-35] developed a technique that couples atomic force microscopy and infrared spectroscopy (AFM-IR), which is based on photothermally induced resonance and is currently the most sensitive technique to measure chemical composition with a spatial resolution of <20 nm. This technique offers tremendous potential to explore the conformational changes of extracellular proteins and cell proteins in the area surrounding internalized nanoparticles.

In AFM-IR, a sample is placed on a transparent, total internal reflective surface e.g. zinc selenide, which is illuminated by a pulsed and tunable IR laser. If the evanescent field excites molecular vibrations in the sample, a small thermal expansion is induced. This expansion is detected by the AFM tip which serves as a near field detector and results in the oscillation of the AFM cantilever. The resultant cantilever oscillations are sensed by reflecting a second laser beam off the top surface of the cantilever onto a four-quadrant detector (Figure 1). These oscillations are recorded as a cantilever ringdown signal. Fourier transformation of this signal generates a signal amplitude corresponding to the IR-absorption[32-37]. Furthermore, the resonance frequency of these oscillations indicates the nanomechanical properties (stiffness) of the sample. The measurement of the frequency helps in localizing the nanoparticles, which typically have a different stiffness than the biological structures. This technique has lateral resolution in the range of 10 nm to 50 nm[32, 37]. These features make AFM-IR a valuable tool for investigating nanoparticle–cell or nanoparticle–protein interactions.

Nanoscale sp[3] carbon based nanomaterial[38] i.e. nanodiamonds (NDs) is one of the most explored carbon-based nanoparticles in recent years. It retains the unique properties of bulk diamonds at the nanoscale, which is attributable to its hardness and Young's modulus, optical and fluorescence properties, high thermal conductivity, electrical resistivity and chemical stability[39,40]. Owing to its properties, NDs have been used in a wide variety of applications such as magnetic resonance imaging[41], chromatography[42,43], mass spectrometry[44], tribology and lubrication[45], nanocomposites[46,47], surgical implants and tissue scaffolds[48], biomedical imaging and drug delivery[1,49-51]. Detonation techniques, laser ablation, high energy ball milling at high pressure and temperature, plasma-assisted chemical vapour deposition, autoclave synthesis from supercritical fluids and chlorination of carbides are some of the commonly used manufacturing approaches[39]. The broad application of NDs, compounded with differing manufacturing techniques must raise concerns of increased and variable human and environmental exposure to these nanomaterials. Some studies have highlighted that NDs can induce conformational changes in protein structures, but this was confirmed only at macro and micro levels. It was found that when bovine serum albumin was exposed to NDs, α-helical content decreased and β-turn and β-sheet structures increased[29]. It was also shown that the smaller the size (5 nm *vs.* 50 nm) of the ND, the greater the effect on conformation changes (the loss of functionality) of lysozyme[27,28]. Similarly, Svetlakova *et. al.* reported that ND induces conformational changes in human serum albumin with the cleavage of disulfide bridges, modification of H-bonding in tyrosine residues and an increase in random coil formation[52]. Given their applications in the biomedical field, and many reported incidence of protein conformational changes, precise understanding of how these and other nanoparticles interact with biological systems is vital to assure patient safety.

In this study we focus solely on the investigations of the impact of NDs (model nanoparticle) on the conformation of intracellular proteins (proteins inside liver cell) and extracellular protein (fibronectin-FN) using AFM-IR spectroscopy. Since the liver is the primary site of nanoparticle uptake and localization, the investigation of the effect of NDs on liver cells may possibly highlight their impact on overall health. In addition, nanoscale characterization of cellular protein structures after uptake of nanoparticles would provide deeper understanding of the mechanism of protein denaturation. We demonstrated that NDs induced conformational changes in both extracellular and intracellular proteins. Increased β-sheet content and possible denaturation of proteins were observed after the exposure of intra- and extracellular proteins to the NDs.

EXPERIMENTAL SECTION

Materials

Rat hepatoma (Fao cell) cultured in Dulbecco's Modified Eagle's Medium (DMEM) supplemented with 4500 mg/L D-glucose, 2mM L-glutamine (Sigma-Aldrich, Australia), Penstrep® (100 IU mL^{-1} penicillin, 100 μg.mL^{-1} streptomycin: Gibco, Life Technologies, USA) and 10% Fetal Bovine Serum (Sera Laboratories, UK) was used to prepare both 2D and 3D liver cell culture models.

Physico-chemical Characterization

Nanodiamond (ND) produced by laser assisted technology[53] with mean size of 4-5 nm (Ray Techniques Ltd, Israel) were used in the study. Physicochemical properties of ND were characterized with Fourier transform infrared spectroscopy (FTIR), X-ray diffractometry (XRD), atomic force microscopy (AFM), transmission electron microscopy (TEM) and X-ray photoelectron spectroscopy (XPS), (Figure 2).

The diffraction characteristics of ND was determined by XRD (D8 Advance, Bruker diffractometer- Bruker, UK) in a flat plate geometry using Ni-filtered Cu Kα radiation and a Bruker Lynx eye detector. The X-ray diffraction patterns were acquired from 10 to 100° 2θ with a step size of 0.02° and a count time of 0.1s.

Size and morphology of the ND were assessed with TEM (Philips CM 120- Biofilter, The Netherlands) and AFM (nanoIR™, Anasys Instruments, USA). For the AFM studies, ND was first immobilised on freshly cleaved mica functionalised with poly-L-lysine and scanned in AC mode using a silicon nitride cantilever with a spring constant of 40 Nm^{-1} (EXT125, AppNano, Mountain View, CA, USA) at a scan rate of 0.50 Hz. The images were processed using the Analysis Studio™ software (Anasys Instruments, USA).

Elemental composition of ND particles was characterized using XPS (Axis ultra XPS/ESCA–Kratos Analytical, UK) using an Al-Kα monochromator X-ray source. Survey scan was acquired at 100 eV pass energy between 0 and 1400 eV. High resolution spectra for carbon, oxygen and nitrogen were collected at 20 eV pass energy. The elemental composition (atomic concentration) was calculated from the high resolution spectra using CasaXPS. The measurements were done in triplicate.

Bulk chemical composition (micron scale) was measured using FTIR attenuated total reflectance (ATR). Spectra of the nanodiamond powder were collected on a FTIR7000 series spectrometer (Digilab, USA) with a Germanium internal reflection element (IRE) of 45° incidence angle and using a globar source. Mid-IR absorbance spectra were acquired from 4000 to 400 cm^{-1} at a spectral resolution of 4 cm^{-1} taking the average of 500 scans.

Magnetic printing of 3D cell culture model; to investigate the toxicity of ND in 3D environment we fabricated cell spheroids (3D models) using previously published methodology[49,54,55]. Briefly, cells were first incubated with magnetic nanoparticles (NanoShuttle™PL (NS), n3D Bioscience, USA) at a concentration of 8 μL.cm^{-2} overnight and then levitated magnetically overnight to obtain 3D cellular aggregates. Next, cell aggregates were dispersed and biopatterned into spheroids using magnetic pin drives (Figure S1).

Measurement of cell viability in 2D and 3D; Fao cells cultured in 2D monolayer were treated with ND (prior to treatment, ND dispersion in sterile deionised water was sonicated with ultrasonic probe for 1 h) at concentrations of 10, 25, 50 and 100 μg.mL^{-1} over the period of 48 h and cultured up to four days to detect longer term effects of ND on cell growth. Viability of cells exposed to ND were assessed using Cell Counting Kit-8 (CCK-8) (Dojindo Molecular Technologies, Inc., Santa Clara, CA) as per manufacturers' protocols. The viability of cells within the bioprinted spheroids after treatment with ND for 24 h was evaluated using live/dead assay (PromoCell, Germany) as per the manufacturer's protocol.

BIOSPECTROSCOPY – AFM-IR

AFM-IR – intracellular protein analysis – sample preparation; for the investigation of intracellular protein analysis, spheroids treated with ND at a concentration of 25 μg.mL^{-1} were used. As a control, cell spheroid treated with NS only and Fao cell pellet obtained after centrifugation of cells cultured in monolayer up to 80% confluency were used.

ND treated spheroid, NS loaded spheroids and control cell pellet were fixed in 2.5% glutaraldehyde in 0.1 M phosphate buffer (pH 7.4) for 30 minutes and dehydrated in ethanol (30-100%). Dehydrated spheroids and cell pellet were embedded in Spurr's resin (ProScitech, Australia). Resin-embedded samples were microtomed using glass knives (UltraCut S, Leica Microsystem GmbH, Vienna, Austria) to obtain a semi thin (500 nm) sections. Next the sections were transferred to zinc selenide prisms for biospectroscopic analysis via AFM-IR.

AFM-IR – extracellular protein analysis – sample preparation; human plasma fibronectin (FN) (>95% purity, Sigma Aldrich) was reconstituted and was diluted to 20 μg.mL^{-1} solution in deionised water**.** The ND–FN samples were prepared by adding 150 μL of 1 mg.mL^{-1} ND dispersion in deionised water to 1.5 mL of 20 μg.mL^{-1} FN solution. The ND dispersion was sonicated for 1 h using an ultrasonic probe before being added to the protein solution. The ND–FN solution was mixed at 25°C using a vortex mixer for 2 h. Next the solution was centrifuged at 13000 rpm at 4°C for 15 min. 10 μL of supernatant was transferred to the zinc selenide prism to investigate conformational changes in non-adsorbed FN. The remaining supernatant was removed and the FN–ND pellet was rinsed with deionised water three times followed by centrifugation to remove free FN. The pellet was redispersed in deionised water and then transferred to the zinc selenide prism and dried under nitrogen gas. The sample was stored in a desiccator to remove the adsorbed moisture prior to AFM-IR measurements. Control pristine FN sample (20 μg.mL^{-1}) and FN supernatant were transferred to the zinc selenide prism and dried under the nitrogen gas followed by desiccation prior to spectra acquisition.

Nanoscale infrared biospectroscopy was carried out using AFM-IR instrument, nanoIR™, (Anasys instruments, USA). Prior to the acquisition of the spectra, four IR background spectra were collected from 1000 to 1800 cm^{-1}. These spectra were averaged and normalized to calibrate the signal intensity as a function of wavenumber. The second cantilever oscillation mode was chosen for optimizing the cantilever ringdown signal at its frequency centre of 185 kHz using a frequency window of 20 kHz. The infrared laser focus was optimized at 1550 cm^{-1}, 1620 cm^{-1}, 1640 cm^{-1}, 1690 cm^{-1} and 1723 cm^{-1} for cell-based samples (ND-treated spheroid sections, NS treated spheroid and control cell sections) as well as for extracellular protein-based samples (FN, FN–ND and FN supernatant). Co-averages of 256 scans were used for optimization. The laser power was adjusted to obtain a clean and distinct 'IR-hotspot' in the centre of the image which corresponds to the location where the AFM tip is in contact with the sample (Figure S5).

AFM-IR spectra were collected from 1300 cm^{-1} to 1800 cm^{-1} at 1 cm^{-1} intervals, co-averaging a total of 256 cantilever ringdown signals at each wavenumber. The laser source produces 10 ns pulses at a repetition rate of 1 kHz. The spectral resolution is determined by the laser line width and is estimated to be 8 cm^{-1} in this spectral range. A minimum of ten
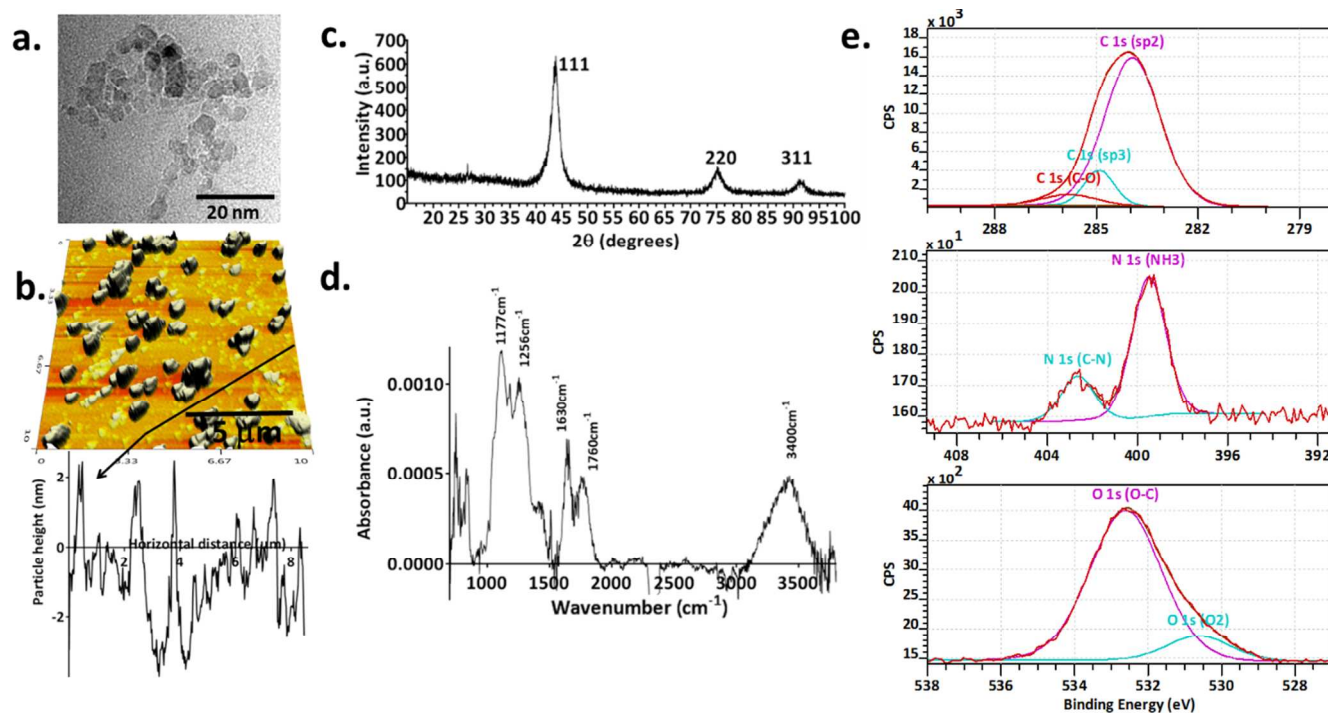
Figure 2. Physicochemical characterization of nanodiamond (ND): a) TEM image of ND particles showing the individual particles in the range of 4-5 nm with cuboidal shape; b) AFM height image of ND particles showing aggregates and individual nanoparticles; The profile analysis insert below the image show the height of the particles in the range of 4 nm; c) XRD graph showing key diamond peaks at 2θ of 111, 220 and 311. Grain size was determined to be around 4-5 nm; d) FTIR spectra collected from the bulk of ND indicated the presence of key diamond peaks in the region of 1117-1256 cm^{-1}; e) XPS spectra collected from NDs showed peaks related to carbon, oxygen and nitrogen. Elemental analysis showed 78.77% carbon, 8% oxygen and 1.7% of nitrogen.

spectra were collected across each sample, spectra were presented either as an array spectra to show spatial locations or were averaged and plotted for analysis. IR images/maps of the samples were collected in contact mode at a scan rate of 0.1 Hz with a co-average of 16 using a silicon nitride cantilever with a nominal spring constant of 0.5 Nm^{-1} (EXC450 tips, AppNano, Mountain View, CA, USA). All spectral analyses were undertaken after normalization using GRAMS software (ThermoFisher, Waltham, MA, USA), Essential FTIR software (Operant LLC, USA) and Analysis Studio™ software (Anasys Instruments, USA). Spectral subtraction was used to show differences between the spectra of the samples. All the spectra collected from cell samples (ND treated, NS treated, and control cell; Figure 3g) were processed in GRAMS software, smoothing being achieved with a polynomial function on 5 points. The spectra presented in Figure 4 were processed in the Essential FTIR software: using Savitzky-Golay smoothing with a quadratic/cubic 25pt function. The endpoints were extrapolated then truncated. All subtractions were performed by manually adjusting the subtraction factor applied to the epoxy spectrum. The subtraction factors used were different for each set of samples, but exactly the same subtraction factor was used within a given sample set. All subtractions were performed on smoothed spectra. Figure S4 spectra were processed in Analysis Studio™ software and smoothing was done using with a polynomial order of 2 on 25 points. Similarly spectra collected from FN-ND, non-adsorbed FN, and FN only (Figure 5) were processed in the Analysis Studio™ software and smoothed using a polynomial function of 2 and 5 points.

RESULTS AND DISCUSSION

Physical properties; XRD diffraction pattern of ND revealed diffraction maxima at the 2θ of 43.9 and 75.4, which correspond to diamond peaks[53]. The average grain size of diamond crystallites, estimated using the Scherrer formula, was 5 nm. The absence of non-diamond peaks and troughs in the spectra indicate high sample purity. TEM and AFM images of nanoparticles showed that they were cuboidal in shape and the size of individual particle was on average 3-5 nm, which was in agreement with the XRD results (Figure 2a, b and c).

Chemical properties; FTIR spectra collected from the bulk ND (Figure 2d) revealed typical ND peaks at 1107 cm^{-1}, 1177 cm^{-1} and 1256 cm^{-1}, which are due to stretching vibration of a C-O group[56]. Low intensity peaks were observed at 1384 cm^{-1} and 1436 cm^{-1}, which are associated with the aceto-group and C-H (SP$_3$) bending vibration. Presence of aceto group may be due to contamination of ND during the laser assisted manufacturing stages[56]. Furthermore, the presence of a peak at 1760 cm^{-1} (C=O) indicates that nanoparticles were partly oxidized, while the peak at 1630 cm^{-1} corresponds to the bending vibration of adsorbed water. The broad peak at 3400 cm^{-1} corresponds to an OH-stretching vibration. This indicates the adsorption of water on ND[57,58].

XPS measurement for ND confirmed the presence of three elements: carbon (C 1s), oxygen (O 1s), and nitrogen (N 1s). Deconvolution of the carbon (C 1s) peak of high resolution XPS spectra showed the presence of the main peaks at E$_b$=283.95 eV, E$_b$=284.96 eV and E$_b$=286.23 eV, which
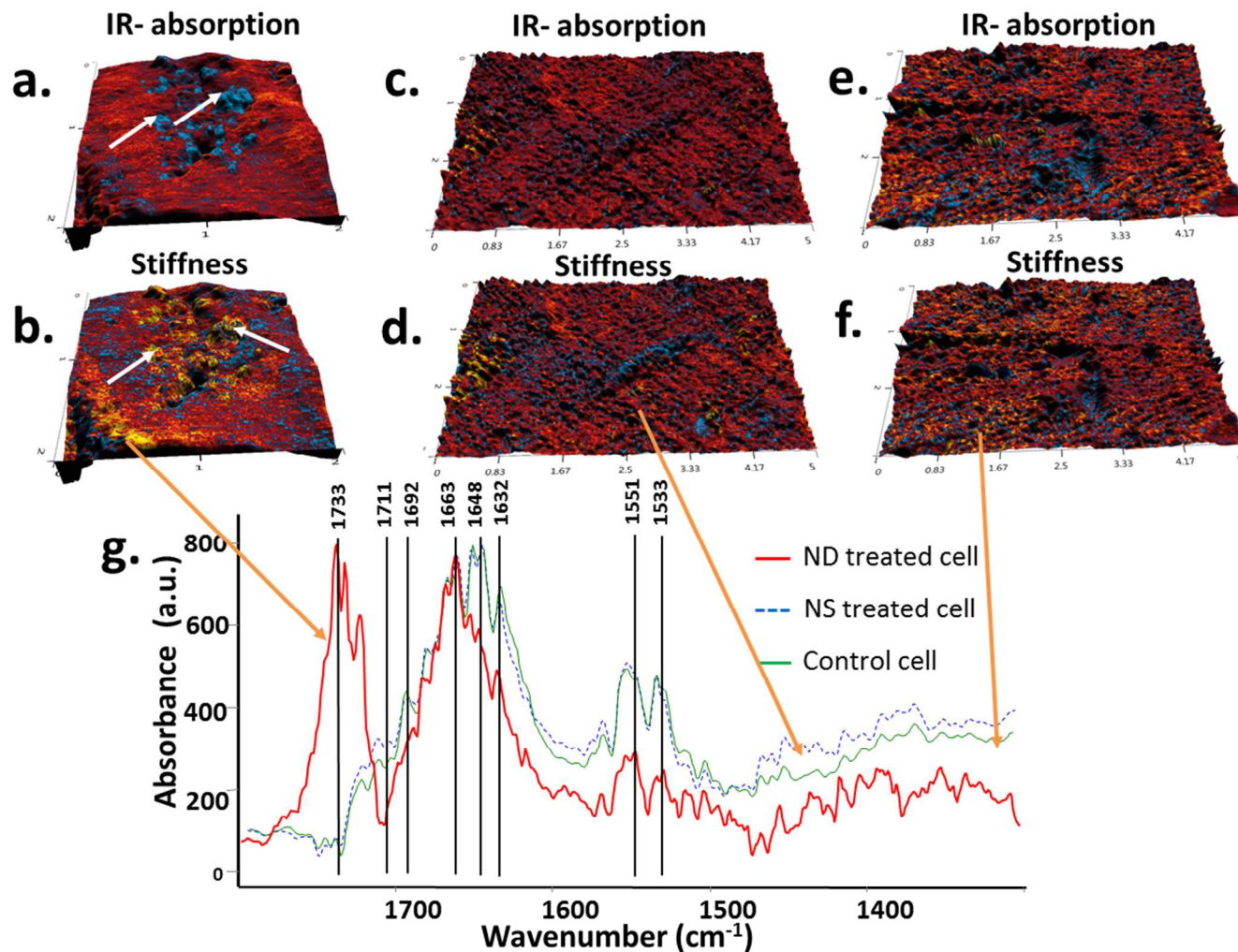
Figure 3. Topographical image, map of nanochemical and nanomechanical properties of a section of spheroid treated with ND, NS and control cells: a) AFM-IR absorbance map (2 μm x 2 μm) of the ND treated spheroid section at 1640 cm^{-1} showing inhomogeneous absorbance pattern, blue spots (white arrows) are the regions with lower absorbance (ND localised area) and red regions are the regions of higher absorbance (cellular region); b) corresponding nanomechanical map of ND-treated cell indicated that the region of lower absorbance at 1640 cm^{-1} had higher stiffness (yellow spots, white arrows); c) AFM-IR absorbance map (3 μm x 5 μm) of the NS treated spheroid section at 1640 cm^{-1}; d) nanomechanical map of NS treated spheroid section; e) AFM-IR absorbance map (3 μm x 5 μm) of control cell section acquired at 1640 cm^{-1} ; f) nanomechanical map of control cell; g) corresponding averaged AFM-IR spectra collected from ND - treated cell, NS-treated and control cell section. All the spectra collected from individual samples were averaged, normalised and smoothed to 5 points with a polynomial function.

correspond to the sp^3 (diamond), sp^2 hybridized carbon species and oxygen containing groups (C-O) respectively[59]. Deconvolution of the oxygen (O 1s) peak showed the peak at E_b=530.6 eV associated to (C-O) and peak at E_b=532.5 eV corresponding to water adsorbed to the ND surface. The presence of oxygen (8%) indicated partial oxidation of the ND, which was in agreement with the FTIR results. Additionally, a small amount of nitrogen (1.7%) was detected on the surface. Nitrogen spectra had two main peaks that correspond to NH$_3$ (E_b=399.5 eV) and N-C (E_b=402.6 eV). The presence of nitrogen could be associated to the contaminants from the manufacturing process.

Effect of ND on cell viability

To select the concentration of ND to interrogate ND–protein interactions we evaluated *in vitro* cytotoxicity of ND using cells cultured in 2D monolayer. Cells were treated with ND at different concentrations (10, 25, 50 and 100 μg.ml^{-1}) for 48 h

and metabolic activity of the cells, which corresponds to the viability of cells, was measured. The results obtained showed no significant differences in viability of cell up to the concentration of 100 μg.mL^{-1} for 48 h (Figure S2c). Extended incubation time (four days) resulted in a decrease in viability with increasing concentration of ND, in particular, 25 μg.mL^{-1} resulted in 24% drop of viability, while 50 and 100 μg.mL^{-1} resulted, respectively, in 37% and 44% of cell viability drop (Figure S2c). In addition, cell viability was assessed in 3D (spheroids) using live/dead assay prior to ND–protein interaction studies. Results of live/dead assay showed that the majority of cells were viable within the spheroid up to the concentration of 25 μg.mL^{-1} (Figure S2b) and the diameter of the spheroid which also indicates viability of cells in 3D culture[55,60] was similar to control sample. The diameter increased (dilation of the spheroid that suggests a drop in viability) for the higher concentrations of ND (Figure S2a). Based on both assays, 25 μg.mL^{-1} ND was selected as a concentration for .
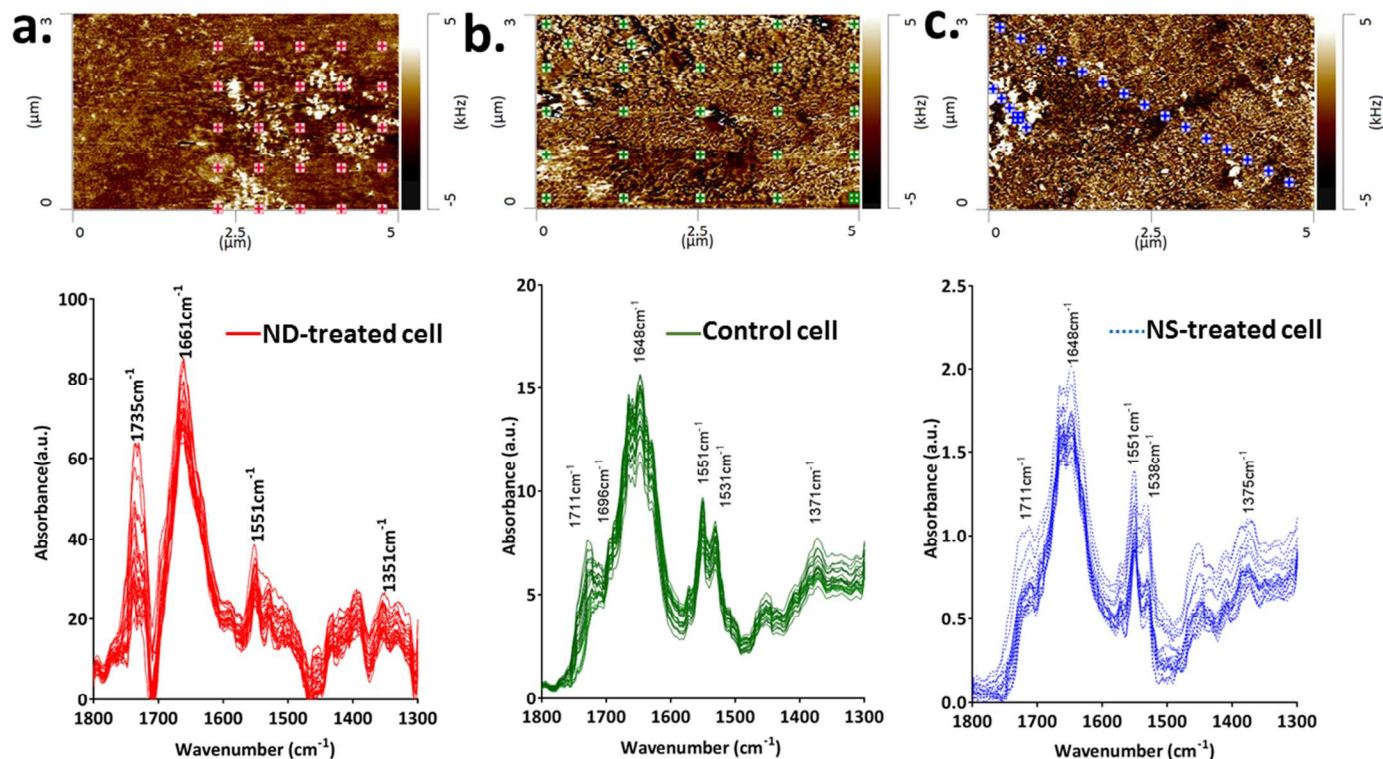
Figure 4. a) AFM-IR array of spectra collected from ND-treated Fao cells with the corresponding contact resonance peak frequency image. The amide I peak maxima was observed at 1661 cm⁻¹, indicating a transition towards increased β-sheet content. The intensity of peak at 1735 cm⁻¹ was found to increase closer to the ND particles suggesting conformational changes in protein structure after the uptake of ND particles; b) AFM-IR array of spectra collected from NS-treated cells with corresponding frequency image; c) AFM-IR array of spectra collected from control cells with the corresponding frequency image. Both the control and NS-treated cell had an amide I maxima at 1648 cm⁻¹, indicating higher α-helical content and peak at the 1735 cm⁻¹ was not present.

which cells remain viable.

Effect of ND on intracellular protein

Since the development of AFM by Binnig *et. al.*[61], this technique has been widely applied in nano and atomic scale imaging and probing with high spatial and temporal resolutions[62,63]. AFM-IR offers dual capability of scanning probe microscopy and nanoscale IR spectroscopy, which is capable of detecting both nanochemical and nanomechanical characteristics. This technique is based on the localized thermal expansion of a sample after absorbing infrared light of a specific wavenumber. Thermally induced geometrical changes (at the nanoscale) are detected by the deflection of the AFM cantilever that remains in contact with the sample. The measurement of these changes makes it possible to distinguish materials with different coefficient of thermal expansion (CTE). Because of the low CTE of ND (1.18×10^{-6} K⁻¹)[64], it undergoes minimal expansion when exposed to the pulsed laser, which was confirmed by the AFM-IR spectra collected from pristine ND (Figure S3a).

Differences in CTE between ND and surrounding cellular structures (115×10^{-6} K⁻¹)[65] enable the identification of the NDs inside the ND-treated cells (Figure 3a) by acquiring AFM-IR absorbance map at 1640 cm⁻¹ which corresponds to the amide I band of protein. Regions of a very low absorbance, were evidenced on the samples and these regions corresponded to NDs (Figure 3a). Absorbance maps at 1640 cm⁻¹ were also collected for NS-treated cell and control cell (Figure 3c, 3d), but low absorbance regions were not observed for these samples. These findings were preliminary evidence for the

uptake of ND into the cell. Furthermore, the stiffness of the low absorbance region in the ND-treated cell was also higher when compared to the surrounding cellular region (Figure 3a, 3b). These results, combined with the similar cuboidal morphology of the NDs as determined by TEM and AFM, confirmed the uptake of ND by the cells. While, one might suspect that these geometrical features and changes to IR amplitude could be associated with NS that were used to levitate the cells, our control experiments on the NS-treated cells and cells only samples showed a lack of such features (Figure 3c and 3d). Furthermore, NS are functionalised with poly-L-lysine and the AFM-IR spectra of NS showed distinct peaks at 1641 cm⁻¹ for poly-L-lysine (Figure S3b). If the features observed for ND-treated samples were NS then some absorbance signal at 1640 cm⁻¹ would have been apparent, which was not confirmed here. For the NS-treated samples, some regions of higher stiffness (Figure 3d) were observed, however these zones had absorbance in 1640 cm⁻¹, which excludes the existence of ND. Taken together, the presented results provide strong evidence that the cuboidal features detected for ND-treated samples were associated with ND particles.

Having confirmed the uptake of ND into the cells, the potential of ND to induce protein conformational changes was investigated by collecting AFM-IR spectra of the ND-treated, NS-treated and control cells. Should the NDs induce any conformational changes, a change in the AFM-IR spectra should be expected. The averaged spectra recorded for ND-treated cells (Figure 3g) had an amide I absorption maxima at 1663 cm⁻¹ with a shoulder at 1692 cm⁻¹ (Figure 3g), indicating
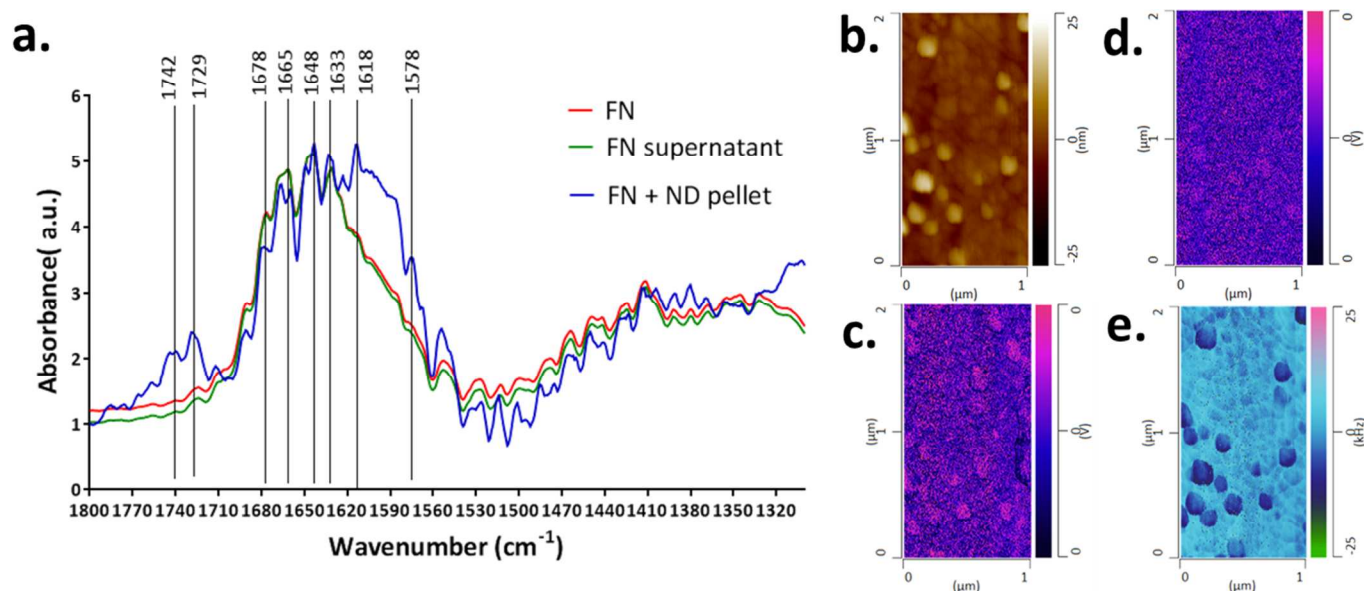
Figure 5: a) AFM-IR spectra collected from pure fibronectin (FN), non-adsorbed fibronectin (FN supernatant), and adsorbed fibronectin (FN+ND pellet). Broadening of peak in amide I region with absorption maxima at 1618 cm^{-1} and appearance of peak at 1729 cm^{-1} was observed in FN-ND sample which corresponds to aggregation of FN and protonation of –COO$^-$ group present in FN respectively. Peak broadening and peak at 1729 cm^{-1} was not evident in both the FN and FN supernatant samples; b) Topographical image showing cuboidal ND particles; c) AFM-IR absorbance map acquired at 1620 cm^{-1} showed regions of higher absorbance (bright pink spots) which correspond to the sites of protein denaturation and aggregation; d) absorbance map at 1723 cm^{-1} shows zones of absorbance (bright pink regions) indicating possible sites where protonation of FN occurred; e) Stiffness map indicated localised softness (dark blue spots) due to the adsorption of protein on ND particles.

transition of protein conformation from α-helical to the β-sheet and β-turn like structures[37]. On the contrary, both spectra for NS-treated cells and control cells (Figure 3g) had amide I absorption maxima at 1648 cm^{-1}, depicting high α-helical content. Further evidence for conformational changes in the protein structure can be found by comparing the peak intensity ratio of the amide I peak to the amide II peak (Figure 4a, 4b and 4c). The amide I (1661 cm^{-1}) to amide II (1551 cm^{-1}) peak intensity ratio of the ND treated cell is 2.64 (Figure 4a), while the ratio for the NS and control cell (1648 cm^{-1}:1551 cm^{-1}) was 1.5-1.6 (Figure 4b and 4c). The change in this ratio could have been caused by ND-induced oxidative stress inside the cells[24,25,26]. The oxidative stress has been reported to result in carbonylation of intracellular proteins and cause aggregation, conformational change and even total loss of protein functionality[66]. This process has been observed in HeLa cells treated with ND manufactured by detonation techniques[67]. In addition, a high intensity peak at 1735 cm^{-1} was observed in the spectra array collected across the ND-treated cells (Figure 4a), which is not as pronounced in either the control (Figure 4b) or NS-treated (Figure 4c) cells. The peak intensity at 1735 cm^{-1} increased in the close vicinity of ND localization (Figure 4a) indicating the localized effect of ND on conformational changes in the protein structure. The increased intensity of this peak (1735 cm^{-1}) that indicates the alternation of the protein structure was caused by the deep conformational changes due to protein denaturation, which could have happened due to two reasons: (i) the breakage of hydrogen bond in the protein structure upon the adsorption to the nanoparticle surface, and (ii) the protonation of –COO$^-$ group in the proteins[68] (Figure 4a). The protonation may be due to two processes. Firstly, it may be the result of protein denaturation causing a change in pKa near the ND-protein interface. Secondly, it may occur due to the direct interaction between the protein and substrate with low dielectric permittivity. The ND's low dielectric permittivity (ε) of 8.7[69] could potentially lead to a shift of the carboxyl group's dissociation equilibrium toward the neutral protonated species. However, without further study, it is uncertain whether protein denaturation or direct ND interaction, or a combination of both, is responsible for the protonation.

Nanodiamond–extracellular protein interactions. To confirm the impact of ND on protein's conformation we selected additionally an extracellular protein, fibronectin, and investigated its conformational changes when exposed to ND using the AFM-IR. FN is present in plasma as well as the cell surface and is secreted primarily by liver hepatocytes. It plays a key role in cell proliferation, migration, wound healing and is involved in the opsonisation of nanoparticles[70,71]. FN is also known to be susceptible to conformational changes after adsorption to a substrate, which makes this protein an ideal model to study ND-protein interactions.

AFM-IR spectra were collected from FN adsorbed to ND (FN-ND), FN supernatant, and FN. Much like the previous case with Fao cells, conformational changes should alter the AFM-IR spectra. The spectra from all three samples had three peaks in common, the amide I peaks at 1633 cm^{-1} and 1648 cm^{-1}, along with a shoulder peak at 1678 cm^{-1} (Figure 5a). All these peaks correspond to high β-sheet and β-turn components within the secondary structure of FN[72]. This is in agreement with the literature, where FN has been reported to have majority of secondary protein structure in the β-strand conformations[73]. However, when FN was adsorbed to NDs (FN-ND), an additional amide I peak with absorption maxima at 1618 cm^{-1} was observed, which was not evident in the FN-

supernatant and FN control samples (Figure 5a). The appearance of such a peak is associated with the multimerization and aggregation of proteins[74]. In the case of FN, the aggregation occurs due to intermolecular hydrogen bonding, ultimately leading to intermolecular β-sheet formation[74]. The initial hydrogen bonding between monomeric FN is only possible if the FN undergoes denaturation as a result of adsorption to ND. This finding is in agreement with the study where temperature-induced denaturation of FN resulted in the formation of FN aggregates[74]. Additionally, in the case of FN-ND sample, a prominent peak at 1729 cm^{-1} was observed which corresponds to the protonation of –COO$^-$ group in the FN structure, similar to ND-treated cells. The protonation of –COO$^-$ confirms the conformational changes and possible denaturation of the FN[72,75,76].

In order to identify the regions where conformational change occurred after adsorption to ND, absorbance maps were collected for FN-ND at 1620 cm^{-1} (Figure 5c) and 1723 cm^{-1} (Figure 5d). The absorbance map demonstrated zones of higher absorbance (bright pink spots), which corresponds to the sites where structural changes in FN occurred after adsorption to ND. These zones had a cuboidal morphology (Figure 5b), and lower stiffness compared to its surrounding (Figure 5e), suggesting that the ND was coated by FN. In contrast to ND-treated Fao cells, zones around ND for FN-ND showed lower stiffness which was due to the differences in sample preparation. ND-treated Fao samples were microtomed and this process removed proteins from the top surface thus appeared as regions of higher stiffness; AFM probe was in direct contact with bare ND surface. Whereas, microtomy was not required for FN-ND samples and the layer of FN remained around the nanoparticles which resulted in lower stiffness; AFM probe was in direct contact with the protein layer. When an array of spectra were collected from the FN-ND samples, the intensity of the peak at 1725 cm^{-1} was found to be more pronounced closer to the ND particle (Figure S4), which was not evident in both the FN and FN-supernatant samples. This result further confirms that conformational changes and denaturation occurs at the FN-ND interface after adsorption.

Cumulatively our results provide evidence that ND can induce conformational changes in the secondary structure of both intra- and extracellular protein structures. Our results highlighted that ND caused conformational changes and/or denaturation of proteins in its immediate vicinity. These effects may result in the total loss of functionality of the protein at a cellular level and thus may have a negative effect on cell viability and vitality.

CONCLUSION

The high spatial resolution of AFM-IR has enabled the study of both intra- and extracellular protein interactions with individual nanoparticles. For the first time, the interface of internalized nanoparticles was examined using AFM-IR and we demonstrated that proteins, both intracellular and extracellular, underwent conformational changes at the ND-protein interface. These results suggest that individual nanoparticles had negative effects on the protein structure. Despite the fact that AFM-IR does not allow us to determine the concentration at which macroscopic cytotoxicity is induced, the high resolu-

tion data of nanoscale chemistries allowed us to gain a precise understanding of nanoparticles–proteins/macromolecules interactions. This knowledge has a powerful implication for our understanding of nanomaterial toxicity in bodily environment.

As previously explained toxicity of nanoparticles depends on their size, shape and surface chemistry, as well as vary from cell to cell (healthy *vs* malignant). The AFM-IR technique will be fundamental to establish optimal nanoparticle characteristics, including surface conditions, for their safe use in biomedical applications, e.g. drug delivery and bioimaging.

REFERENCES

(1) Alhaddad, A.; Adam, M. P.; Botsoa, J.; Dantelle, G.; Perruchas, S.; Gacoin, T.; Mansuy, C.; Lavielle, S.; Malvy, C.; Treussart, F. *Small* **2011**, *7*, 3087-3095.
(2) Chow, E. K.-H.; Ho, D. *Sci. Transl. Med.* **2013**, *5*, 216rv214-216rv214.
(3) Kaur, R.; Badea, I. *Int. J. Nanomedicine* **2013**, *8*, 203.
(4) Wagstaff, A. J.; Brown, S. D.; Holden, M. R.; Craig, G. E.; Plumb, J. A.; Brown, R. E.; Schreiter, N.; Chrzanowski, W.; Wheate, N. J. *Inorg. Chim. Acta* **2012**, *393*, 328-333.
(5) Baek, S.; Singh, R. K.; Khanal, D.; Patel, K. D.; Lee, E.-J.; Leong, K. W.; Chrzanowski, W.; Kim, H.-W. *Nanoscale* **2015**, *7*, 14191-14216.
(6) Vaijayanthimala, V.; Tzeng, Y.-K.; Chang, H.-C.; Li, C.-L. *Nanotechnology* **2009**, *20*, 425103.
(7) Forest, V.; Cottier, M.; Pourchez, J. *Nano Today* **2015**, *10*, 677-680.
(8) Zhang, S.; Gao, H.; Bao, G. *ACS nano* **2015**, *9*, 8655-8671.
(9) Zhang, X.; Hu, W.; Li, J.; Tao, L.; Wei, Y. *Toxicol. Res.* **2012**, *1*, 62-68.
(10) Chithrani, B. D.; Chan, W. C. *Nano Lett.* **2007**, *7*, 1542-1550.
(11) Chithrani, B. D.; Ghazani, A. A.; Chan, W. C. *Nano Lett.* **2006**, *6*, 662-668.
(12) Chu, Z.; Miu, K.; Lung, P.; Zhang, S.; Zhao, S.; Chang, H.-C.; Lin, G.; Li, Q. *Sci. Rep.* **2015**, *5, 11661, 10.1038/srep11661.*
(13) Favi, P. M.; Gao, M.; Johana Sepúlveda Arango, L.; Ospina, S. P.; Morales, M.; Pavon, J. J.; Webster, T. J. *J. Biomed. Mater. Res., Part A* **2015,** *103*, 3449-3462.
(14) Chowdhury, S. M.; Lalwani, G.; Zhang, K.; Yang, J. Y.; Neville, K.; Sitharaman, B. *Biomaterials* **2013**, *34*, 283-293.
(15) Zeng, K.; Li, J.; Zhang, Z.; Yan, M.; Liao, Y.; Zhang, X.; Zhao, C. *J. Mater. Chem. B* **2015**, *3*, 5249-5260.
(16) Wu, Y.; Tang, W.; Wang, P.; Liu, C.; Yuan, Y.; Qian, J. *Part. Part. Syst. Charact.* **2015**, *32*, 779-787.
(17) Roach, P.; Farrar, D.; Perry, C. C. *J. Am. Chem. Soc.* **2006**, *128*, 3939-3945.
(18) Lynch, I.; Dawson, K. A. *Nano Today* **2008**, *3*, 40-47.
(19) Elsaesser, A.; Howard, C. V. *Adv. Drug Delivery Rev.* **2012**, *64*, 129-137.
(20) Shen, X.-C.; Liou, X.-Y.; Ye, L.-P.; Liang, H.; Wang, Z.-Y. *J. Colloid Interface Sci.* **2007**, *311*, 400-406.
(21) Shang, L.; Wang, Y.; Jiang, J.; Dong, S. *Langmuir* **2007**, *23*, 2714-2721.
(22) Fei, L.; Perrett, S. *Int. J. Mol. Sci.* **2009**, *10*, 646-655.
(23) Ong, K. J.; MacCormack, T. J.; Clark, R. J.; Ede, J. D.; Ortega, V. A.; Felix, L. C.; Dang, M. K.; Ma, G.; Fenniri, H.; Veinot, J. G. *PLoS ONE* **2014**, *9*, e90650.
(24) Li, J.; Strong, R.; Trevisan, J.; Fogarty, S. W.; Fullwood, N. J.; Jones, K. C.; Martin, F. L. *Environ. Sci. Technol.* **2013**, *47*, 10005-10011.
(25) Li, J.; Tian, M.; Cui, L.; Dwyer, J.; Fullwood, N. J.; Shen, H.; Martin, F. L. *Sci. Rep.* **2016**, *6, 20207, 10.1038/srep20207.*
(26) Li, J.; Ying, G.-G.; Jones, K. C.; Martin, F. L. *Analyst* **2015**, *140*, 2687-2695.
(27) Perevedentseva, E.; Cai, P.-J.; Chiu, Y.-C.; Cheng, C.-L. *Langmuir* **2010**, *27*, 1085-1091.
(28) Perevedentseva, E.; Tu, J.; Cheng, C.; Chung, P.; Chang, H.; Cheng, C. *Nanotechnology* **2006**, *2*, 440-443.
(29) Wang, H.-D.; Niu, C. H.; Yang, Q.; Badea, I. *Nanotechnology* **2011**, *22*, 145703.
(30) Downes, A.; Mouras, R.; Elfick, A. *BioMed Res. Int.* **2010**, *2010, 101864, 10.1155/2010/101864.*
(31) Centrone, A. *Annu. Rev. Anal. Chem.* **2015**, *8*, 101-126.

(32) Gruszecki, W.; Kulik, A.; Janik, E.; Bednarska, J.; Luchowski, R.; Grudzinski, W.; Dietler, G. *Nanoscale* **2015**, *7*, 14659-14662.

(33) Dazzi, A.; Prazeres, R.; Glotin, F.; Ortega, J. *Opt. Lett.* **2005**, *30*, 2388-2390.

(34) Dazzi, A.; Prazeres, R.; Glotin, F.; Ortega, J. *Ultramicroscopy* **2007**, *107*, 1194-1200.

(35) Dazzi, A.; Prazeres, R.; Glotin, F.; Ortega, J. *Infrared Phys. Technol.* **2006**, *49*, 113-121.

(36) Katzenmeyer, A. M.; Holland, G.; Kjoller, K.; Centrone, A. *Anal. Chem.* **2015**, *87*, 3154-3159.

(37) Ruggeri, F.; Longo, G.; Faggiano, S.; Lipiec, E.; Pastore, A.; Dietler, G. *Nat. Commun.* **2015**, *6, 7831, 10.1038/ncomms8831.*

(38) Krueger, A. *J. Mater. Chem.* **2008**, *18*, 1485-1492.

(39) Mochalin, V. N.; Shenderova, O.; Ho, D.; Gogotsi, Y. *Nat. Nanotechnol.* **2012**, *7*, 11-23.

(40) Schrand, A. M.; Hens, S. A. C.; Shenderova, O. A. *Crit. Rev. Solid State Mater. Sci.* **2009**, *34*, 18-74.

(41) Manus, L. M.; Mastarone, D. J.; Waters, E. A.; Zhang, X.-Q.; Schultz-Sikma, E. A.; MacRenaris, K. W.; Ho, D.; Meade, T. J. *Nano Lett.* **2009**, *10*, 484-489.

(42) Spitsyn, B.; Denisov, S.; Skorik, N.; Chopurova, A.; Parkaeva, S.; Belyakova, L.; Larionov, O. *Diamond Relat. Mater.* **2010**, *19*, 123-127.

(43) Nesterenko, P. N.; Fedyanina, O. N.; Volgin, Y. V.; Jones, P. *J. Chromatogr. A* **2007**, *1155*, 2-7.

(44) Wu, C. C.; Han, C. C.; Chang, H. C. *J. Chin. Chem. Soc. (Weinheim, Ger.)* **2010**, *57*, 583-594.

(45) Chou, C.-C.; Lee, S.-H. *Wear* **2010**, *269*, 757-762.

(46) Zhang, Q.; Mochalin, V. N.; Neitzel, I.; Hazeli, K.; Niu, J.; Kontsos, A.; Zhou, J. G.; Lelkes, P. I.; Gogotsi, Y. *Biomaterials* **2012**, *33*, 5067-5075.

(47) Luo, X.; Zhang, H.; Cao, Z.; Cai, N.; Xue, Y.; Yu, F. *Carbohydr. Polym.* **2016**, *143*, 231-238.

(48) Brady, M. A.; Renzing, A.; Douglas, T. E.; Liu, Q.; Wille, S.; Parizek, M.; Bacakova, L.; Kromka, A.; Jarosova, M.; Godier, G. *J. Nanosci. Nanotechnol.* **2015**, *15*, 1060-1069.

(49) Souza, G. R.; Molina, J. R.; Raphael, R. M.; Ozawa, M. G.; Stark, D. J.; Levin, C. S.; Bronk, L. F.; Ananta, J. S.; Mandelin, J.; Georgescu, M.-M. *Nat. Nanotechnol.* **2010**, *5*, 291-296.

(50) Wang, D.; Tong, Y.; Li, Y.; Tian, Z.; Cao, R.; Yang, B. *Diamond Relat. Mater* **2013**, *36*, 26-34.

(51) Zhao, L.; Xu, Y.-H.; Akasaka, T.; Abe, S.; Komatsu, N.; Watari, F.; Chen, X. *Biomaterials* **2014**, *35*, 5393-5406.

(52) Svetlakova, A. S.; Brandt, N. N.; Priezzhev, A. V.; Chikishev, A. Y. *J. Biomed. Opt.* **2015**, *20*, 047004-047004.

(53) Zousman, B.; Levinson, O. In *Nanodiamond*; The Royal Society of Chemistry (*Cambridge, UK*) **2014**, pp 112-127.

(54) Timm, D. M.; Chen, J.; Sing, D.; Gage, J. A.; Haisler, W. L.; Neeley, S. K.; Raphael, R. M.; Dehghani, M.; Rosenblatt, K. P.; Killian, T. *Sci. Rep.* **2013**, *3*, 1-8.

(55) Hau, H.; Khanal, D.; Rogers, L.; Suchowerska, N.; Kumar, R.; Sridhar, S.; McKenzie, D.; Chrzanowski, W. *Bioeng. Transl. Med.* **2016**, 10.1002/btm2.10007.

(56) Baidakova, M.; Kukushkina, Y. A.; Sitnikova, A.; Yagovkina, M.; Kirilenko, D.; Sokolov, V.; Shestakov, M.; Vul, A. Y.; Zousman, B.; Levinson, O. *Phys. Solid State* **2013**, *55*, 1747-1753.

(57) Pohl, A.; Joch, S.; Michael, J.; Boschke, E.; Quenzel, P.; Schreiber, J.; Lapina, V.; Opitz, J. In *European Conference on Biomedical Optics*; Optical Society of America *(Washington, DC, USA)*, **2011**, p 80871T.

(58) Wen, C.; Jin, Z.; Liu, X.; Li, X.; Guan, J.; Sun, D.; Lin, Y.; Tang, S.; Zhou, G.; Lin, J. *Guang Pu Xue Yu Guang Pu Fen Xi Guang Pu,* **2005**, *25*, 681-684.

(59) Xie, F.; Xie, W.; Gong, L.; Zhang, W.; Chen, S.; Zhang, Q.; Chen, J. *Surf. Interface Anal.* **2010**, *42*, 1514-1518.

(60) Timm, D. M.; Chen, J.; Sing, D.; Gage, J. A.; Haisler, W. L.; Neeley, S. K.; Raphael, R. M.; Dehghani, M.; Rosenblatt, K. P.; Killian, T. *Sci. Rep.* **2013**, *3, 3000, 10.1038/srep03000.*

(61) Binnig, G.; Quate, C. F.; Gerber, C. *Phys. Rev. Lett.* **1986**, *56*, 930.

(62) Chrzanowski, W.; Lee, J. H.; Kondyurin, A.; Lord, M. S.; Jang, J. H.; Kim, H. W.; Bilek, M. M. *Adv. Funct. Mater.* **2015**, *25*, 339-339.

(63) Haghi, M.; Traini, D.; Wood, L. G.; Oliver, B.; Young, P. M.; Chrzanowski, W. *J. Mater. Chem. B* **2015**, *3*, 2583-2589.

(64) Kidalov, S. V.; Shakhov, F. M. *Materials* **2009**, *2*, 2467-2495.

(65) Frauenfelder, H.; Hartmann, H.; Karplus, M.; Kuntz Jr, I.; Kuriyan, J.; Parak, F.; Petsko, G. A.; Ringe, D.; Tilton Jr, R. F. *Biochemistry (Mosc.)* **1987**, *26*, 254-261.

(66) Castro, J. P.; Ott, C.; Jung, T.; Grune, T.; Almeida, H. *Free Radic. Biol. Med.* **2012**, *53*, 916-925.

(67) Mytych, J.; Lewinska, A.; Bielak-Zmijewska, A.; Grabowska, W.; Zebrowski, J.; Wnuk, M. *Chem. Biol. Interact.* **2014**, *220*, 51-63.

(68) Pitt, W. G.; Spiegelberg, S. H.; Cooper, S. L. In *Proteins at Interfaces*; American Chemical Society *(Washington, DC, USA)* 1987, pp 324-338.

(69) Batsanov, S. S.; Gavrilkin, S. M.; Batsanov, A. S.; Poyarkov, K. B.; Kulakova, I. I.; Johnson, D. W.; Mendis, B. G. *J. Mater. Chem.* **2012**, *22*, 11166-11172.

(70) Mosher, D. F.; Furcht, L. T. *J. Invest. Dermatol.* **1981**, *77*, 175-180.

(71) Pankov, R.; Yamada, K. M. *J. Cell Sci.* **2002**, *115*, 3861-3863.

(72) Michael, K. E.; Vernekar, V. N.; Keselowsky, B. G.; Meredith, J. C.; Latour, R. A.; García, A. J. *Langmuir* **2003**, *19*, 8033-8040.

(73) Patel, S.; Chaffotte, A. F.; Amana, B.; Goubard, F.; Pauthe, E. *Int. J. Biochem. Cell Biol.* **2006**, *38*, 1547-1560.

(74) Pauthe, E.; Pelta, J.; Patel, S.; Lairez, D.; Goubard, F. *Biochim. Biophys. Acta, Protein Struct. Mol. Enzymol.* **2002**, *1597*, 12-21.

(75) Giroux, T. A.; Cooper, S. L. *J. Colloid Interface Sci.* **1990**, *139*, 351-362.

(76) Halter, M.; Antia, M.; Vogel, V. *J. Control. Release* **2005**, *101*, 209-222.

ASSOCIATED CONTENT

Supporting Information

The Supporting Information Available: [Additional figures showing; the schematic process for magnetic bioprinting of spheroids., the assessment of viability of cells in the spheroid, AFM-IR spectra of nanodiamond treated cell, pristine nanodiamond and Nanoshuttle®, AFM-IR array spectra of fibronectin, fibronectin adsorbed to nanodiamond and unadsorbed fibronectin.and optimisation of laser position prior to collection of spectra.] This material is available free of charge via the Internet at http://pubs.acs.org.

AUTHOR INFORMATION

Corresponding Author

* **Email:** wojciech.chrzanowski@sydney.edu.au.; Phone: +610 29351306

Notes
The authors declare no conflict of interest.

Insert Table of Contents artwork here